Comparison of low-amplitude oscillatory shear in experimental and computational studies of model foams

Micah Lundberg,[1] Kapilanjan Krishan,[1,2] Ning Xu,[3,4] Corey S. O'Hern,[5,6] and Michael Dennin[1]

[1]*Department of Physics and Astronomy, University of California at Irvine, Irvine, California 92697-4575, USA*
[2]*School of Physical Sciences, Jawaharlal Nehru University, New Delhi 110067, India*
[3]*Department of Physics and Astronomy, University of Pennsylvania, Philadelphia, Pennsylvania 19104-6396, USA*
[4]*James Franck Institute, The University of Chicago, Chicago, Illinois 60637, USA*
[5]*Department of Mechanical Engineering, Yale University, New Haven, Connecticut 06520-8286, USA*
[6]*Department of Physics, Yale University, New Haven, Connecticut 06520-8120, USA*

A fundamental difference between fluids and solids is their response to applied shear. Solids possess static shear moduli, while fluids do not. Complex fluids such as foams display an intermediate response to shear with nontrivial frequency-dependent shear moduli. In this paper, we conduct coordinated experiments and numerical simulations of model foams subjected to boundary-driven oscillatory planar shear. Our studies are performed on bubble rafts (experiments) and the bubble model (simulations) in two dimensions. We focus on the low-amplitude flow regime in which T1 events, i.e., bubble rearrangement events where originally touching bubbles switch nearest neighbors, do not occur, yet the system transitions from solid- to liquidlike behavior as the driving frequency is increased. In both simulations and experiments, we observe two distinct flow regimes. At low frequencies ω, the velocity profile of the bubbles increases linearly with distance from the stationary wall, and there is a nonzero total phase shift between the moving boundary and interior bubbles. In this frequency regime, the total phase shift scales as a power law $\Delta \sim \omega^n$ with $n \approx 3$. In contrast, for frequencies above a crossover frequency $\omega > \omega_p$, the total phase shift Δ scales linearly with the driving frequency. At even higher frequencies above a characteristic frequency $\omega_{nl} > \omega_p$, the velocity profile changes from linear to nonlinear. We fully characterize this transition from solid- to liquidlike flow behavior in both the simulations and experiments and find qualitative and quantitative agreements for the characteristic frequencies.

I. INTRODUCTION

Aqueous foams are collections of gas bubbles that are separated by liquid walls [1], and like other complex fluids, such as pastes, emulsions, and granular media, they exhibit transitions from solid- to liquidlike behavior in the response to applied stress or strain. For small strains, foams behave elastically with stress proportional to strain. Above the yield strain or stress, bubble rearrangements occur and the system behaves as a liquid. In contrast to Newtonian fluids, foams display complex spatiotemporal behavior in response to applied shear including intermittency, shear banding, and nonlinear velocity profiles [2–12]. Despite a number of experimental, numerical, and theoretical studies of driven foams, a fundamental understanding of the response of foam to applied shear is still lacking.

In this paper, we describe a coordinated set of experimental and numerical studies of model two-dimensional (2D) foams undergoing applied oscillatory planar shear to characterize the transition from solid- to liquidlike behavior and from linear to nonlinear velocity profiles. There have been several studies of the response of foam to steady shear; however, most of these have been performed in the Couette geometry in which flow is confined between two concentric cylinders [13]. Instead, we focus on planar shear to avoid the "trivial" transition to nonlinear velocity profiles that stems from the fact that in the Couette geometry the shear stress varies with distance from the center of the shearing cell.

Another distinguishing feature of this work is its focus on *oscillatory* rather than steady shear as the driving mechanism. There are several reasons for selecting oscillatory shear. First, oscillatory shear allows one to control the amplitude independently from the frequency of the driving. When foams (and other complex fluids) are driven by *steady* shear, they exist in a highly fluidized state that is characterized by continuous, often highly correlated bubble rearrangements, or T1 events [1]. In the highly fluidized state, the statistics of T1 events determine the flow curve and control stress fluctuations [14–21]. With oscillatory shear, one can study the low-amplitude flow regime in which particle rearrangement events do not occur, yet the system can transition from solid- to liquidlike behavior and from linear to nonlinear velocity profiles as the driving frequency is increased. Since T1 events can be suppressed when using oscillatory shear at low amplitude, the dissipation between fluid films becomes the dominant relaxation mechanism [22]. Thus, in this regime one can directly probe the dissipation mechanism by tuning the driving frequency.

In this paper, we report on combined experiments and simulations on model 2D foams: bubble rafts in experiments [23] and the bubble model in simulations [24]. Bubble rafts consist of a single layer of bubbles floating on the surface of water. (See Fig. 1 for a snapshot of the bubble raft used in experiments.) Bubble rafts have a storied history as 2D model systems for both crystalline and disordered solids [23,25]. In addition, we have performed a number of studies characterizing these model systems by measuring and quantifying T1 events [26], stress fluctuations [27], velocity pro-
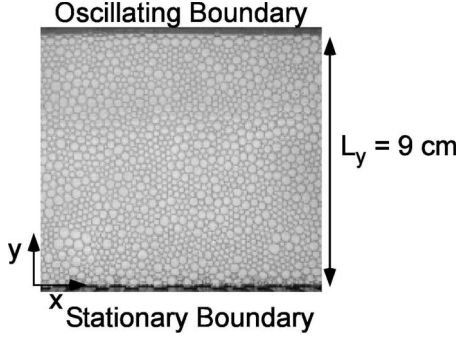
FIG. 1. A typical snapshot of the 2D bubble raft used in experiments with packing fraction $\phi \approx 0.86$ and $N \approx 3700$ bubbles. The bubble raft is composed of a bidisperse distribution of bubble sizes: a 4 to 1 ratio of 2.5 ± 0.3-mm- to 5.3 ± 0.5-mm-diameter bubbles.

files [5–8,28,29], and flow transitions [8]. In this work, experiments on 2D bubble rafts will be compared to simulations of the 2D bubble model introduced by Durian [24]. The bubble model treats foams as soft disks that experience two pairwise forces when they overlap: a repulsive linear spring force proportional to bubble overlap and a dissipative force proportional to velocity differences between bubbles. A useful feature of the bubble model is that it can be generalized to particles with finite mass [6,7]. Thus, the ratio of the damping and inertial forces can be varied to interrogate the damping mechanism. Recent work has shown that the bubble model successfully captures some of the features of the dynamics of bubble rafts under shear, for example, the statistics of individual T1 events [26]. Thus, a comparison of experiments of bubble rafts and simulations of the bubble model in a well-controlled planar shear geometry will allow us to further test under what conditions the bubble model accurately captures the dynamics of model foams.

We will focus on measurements of the total phase shift between the driving wall and interior bubble displacements and on velocity profiles in systems subjected to low-amplitude oscillatory planar shear. At low driving frequencies ω, we observe a nonzero total phase shift, while the velocity profiles rise linearly with distance from the stationary wall. At low frequencies, the total phase shift scales as a power law $\Delta \sim \omega^n$ with $n \approx 3$. In contrast, for frequencies above a crossover frequency $\omega > \omega_p$, the total phase shift Δ scales linearly with the driving frequency. At even higher driving frequencies $\omega_{nl} > \omega_p$, the velocity profiles transition from linear to nonlinear. We compare the two crossover frequencies ω_p and ω_{nl} in the experiments and simulations and find both qualitative and quantitative agreements. The structure of the remainder of the paper is organized as follows: Sec. II presents theoretical background, Sec. III discusses simulation methods, Sec. IV highlights experimental methods, Sec. V describes experimental and simulation results, and Sec. VI presents conclusions.

II. THEORETICAL BACKGROUND

We will now review a simple theoretical treatment of the response of an idealized viscoelastic material to an applied oscillatory strain, which will provide a framework in which to interpret the experimental and simulation results in Sec. V. The main point of this section is to identify the possible flow regimes in viscoelastic materials and their distinguishing properties. For illustration purposes, we have selected the Kelvin-Voigt linear viscoelastic model with frequency-independent elastic modulus and viscosity, although we will discuss how the results from this model can be generalized.

If a planar oscillatory shear strain is applied to a viscoelastic material (with shear along x and shear gradient along y), the x-displacement field $u_x(y)$ of the system relative to the initial positions can be obtained by solving the force balance equation [30]

$$\frac{\partial \Sigma_{xy}}{\partial y} = \rho \frac{\partial u_x^2(y)}{\partial t^2}, \tag{1}$$

where the velocity field is $v_x = \partial u_x / \partial t$ and ρ is the areal mass density. The shear stress Σ_{xy} includes both the elastic and viscous contributions. As mentioned, we will focus on a linear viscoelastic material with

$$\Sigma_{xy} = G\gamma + \eta\dot{\gamma}, \tag{2}$$

where the elastic contribution is proportional to the shear strain $\gamma = \partial u_x / \partial y$ and the viscous contribution is proportional to the shear rate $\dot{\gamma} = \partial v_x / \partial y$. G is the elastic modulus and η is the dynamic viscosity of the material. In general, complex fluids possess complex shear moduli with arbitrary frequency dependence. We have also investigated a frequency-dependent elastic modulus and viscosity, and find that the quantitative scaling of the crossover frequency ω_p depends on the details of the viscoelastic model. However, the qualitative features of the Kelvin-Voigt model, i.e., the existence of ω_p and ω_{nl}, are robust.

We consider the case of parallel plates aligned along the x axis separated by a distance L_y in the y direction as depicted in Fig. 1. The boundary at $y = 0$ is stationary $u_x(0,t) = 0$ (bottom boundary) and the boundary at $y = L_y$ moves according to $x_b(t) = u_x(L_y,t) = A \sin(\omega t)$ (top boundary). The same geometry and notation is used for the experiments and simulations. To solve Eq. (1), we use the ansatz $u_x(y,t) = A(y)\sin(\omega t)$ for the displacement field. Putting these elements together, we find the following solution to Eq. (1) for the displacement field:

$$u_x(y,t) = \text{Im}\left[Ae^{i\omega t} \frac{\sin(ky)}{\sin(kL_y)} \right] \tag{3}$$

and

$$v_x(y,t) = \text{Im}\left[Ai\omega e^{i\omega t} \frac{\sin(ky)}{\sin(kL_y)} \right] \tag{4}$$

for the velocity field. In Eqs. (3) and (4), the wave number k is complex and satisfies the dispersion relation

$$\omega^2 = \frac{Gk^2}{\rho} + i\frac{\eta\omega k^2}{\rho} \tag{5}$$

or

$$k = (\omega \sqrt{\rho}) \frac{(G - i\eta\omega)^{1/2}}{[G^2 + (\eta\omega)^2]^{1/2}}. \tag{6}$$

Distinctive features of the velocity profile are best described by rewriting Eq. (4) in terms of a y-dependent amplitude $v_{mag}(y)$ and local phase $\delta(y)$,

$$v_x(y,t) = v_{mag}(y)\cos[\omega t - \delta(y)]. \tag{7}$$

We define the total phase shift $\Delta \equiv \delta(0) - \delta(L_y)$. Because the flow is periodic, the velocity profile at a given time t repeats at subsequent times separated by period $T = 2\pi/\omega$. To simplify the analysis, we will focus below on velocity profiles at times when the boundary velocity is maximum ($t = 0$ and $v_x(y,0) = v_{mag}(y)\cos[\delta(y)]$). In the simulations and experiments, statistical accuracy was improved by averaging over driving cycles. We defined $v_x(y) \equiv \langle v_x(y, 2\pi p/\omega)\rangle_p$, where $\langle \cdot \rangle_p$ indicates an average over p cycles. Monitoring the full time dependence of the velocity profile is important but is outside the scope of the present work. Error bars on the local phase shift and velocity profile in the simulations and experiments are given by the rms fluctuations within each bin and are typically the size of the data points in the figures unless otherwise noted.

It is instructive to consider two limits of the dispersion relation in Eq. (6): the limit of a pure solid ($G \neq 0$, $\eta = 0$) and the limit of a pure liquid ($G = 0$, $\eta \neq 0$). For the pure solid, we recover the dispersion relation $\omega/k = \sqrt{G/\rho} \equiv v_s$, where v_s is the speed of shear waves in the solid. In this case, $k = \omega/v_s$ is real and the velocity field is a standing wave given by

$$v_x(y,t) = A\omega \cos(\omega t)\frac{\sin(\omega y/v_s)}{\sin(\omega L_y/v_s)}. \tag{8}$$

For $\omega \ll \omega_{nl}^s \equiv v_s/L_y$, $\sin(\omega y/v_s) \approx \omega y/v_s$, and the velocity profile becomes linear in y/L_y, i.e., $v_x(y,t) \approx A\omega \cos(\omega t)y/L_y$. For fixed system size, the transition from linear to nonlinear velocity profiles occurs when $\omega > \omega_{nl}^s$. Because k is real for the case of the pure solid, the total phase shift $\Delta = 0$, and the system oscillates in phase with the driving wall.

In the limit of the pure liquid, we recover the dispersion relation $i\omega = -\nu k^2$, where $\nu = \eta/\rho$ is the kinematic viscosity. In this case, $k = (1 - i)/D$ with $D = \sqrt{2\eta/(\omega\rho)}$. The form of the velocity profile is more complex than that for the pure solid. However, for small driving frequencies the velocity profile can be expanded in powers of L_y/D, and the first term is linear in y/L_y. Thus, for $L_y/D < 1$ or $\omega < 2\omega_{nl}^l$, where $\omega_{nl}^l = \eta/(\rho L_y^2)$, the velocity profiles are approximately linear, as we found for the pure solid. However, in contrast to the pure solid, there is a nonzero total phase shift Δ in the pure liquid since the wave number k is complex. The full form of the phase shift is complicated, but at low driving frequencies one can expand Δ about $\omega = 0$. For the pure liquid, at lowest order in ω, we find that the total phase shift scales linearly with the frequency, $\Delta \sim \omega/6\omega_{nl}^l$.

In Fig. 2, we plot the velocity profiles that satisfy Eq. (1) for two cases: (a) the pure solid ($G > 0$ and $\eta = 0$) and (b) the pure liquid ($G = 0$ and $\eta > 0$). In Fig. 2(a), we show that the
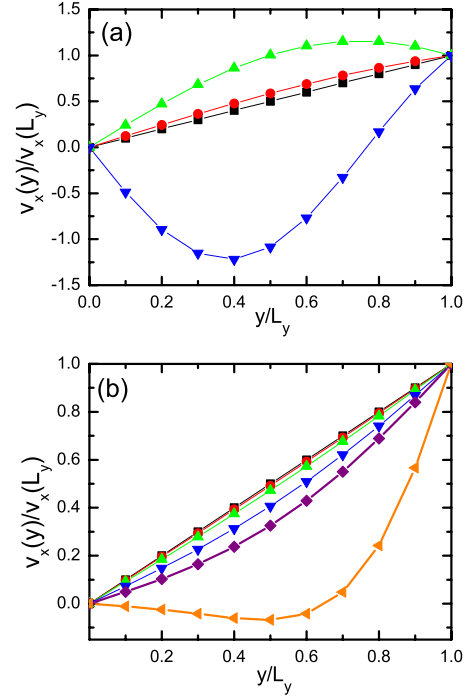

FIG. 2. (Color online) Normalized horizontal velocity profiles $v_x(y)/v_x(L_y)$ at $t = 0$ for the (a) pure solid and (b) pure liquid obtained from solutions to Eq. (1) as a function of the driving frequency ω. We show $\omega/\omega_{nl} = 0.1$ (squares), 1.1. (circles), 2.1 (upward triangles), 4.1 (downward triangles), 6.1 [diamonds, only in (b)], and 20.1 [left triangles, only in (b)]. When referring to the solid (liquid), ω_{nl} corresponds to ω_{nl}^s (ω_{nl}^l).

velocity profiles for the pure solid become nonlinear when $\omega/\omega_{nl}^s > 1$. Note that the profiles first become nonlinear by developing negative curvature above the linear profile, and then as the frequency is increased further the profile develops positive curvature below the linear profile. This nonmonotonic behavior is caused by the standing-wave solution in Eq. (8). In Fig. 2(b), the velocity profile for the pure liquid begins to deviate from a linear profile when $\omega > 2\omega_{nl}^l$. In contrast to the pure solid, the liquid system only exhibits monotonically decaying nonlinear velocity profiles with a "decay length" that decreases continuously with increasing driving frequency. An interesting feature of these profiles is that one can observe negative velocities at sufficiently high frequencies as in the case of the pure solid.

We now consider the solution to Eq. (1) for the velocity profile in the more general case of a viscoelastic material with nonzero G and η. In Fig. 3, we show an expanded range of driving frequencies for a viscoelastic material with $\beta \equiv (\omega_{nl}^s/\omega_{nl}^l)^2 = G\rho L_y^2/\eta^2 = 1$, so that $\omega_{nl}^s = \omega_{nl}^l$. Similar to the case of the pure solid, when $\omega \gtrsim \omega_{nl}^s$ the velocity profiles show a small negative curvature with the profile slightly above the linear profile at $\omega/\omega_{nl}^s = 0.1$. At higher frequencies, the system behaves similar to the pure liquid with monotonically decaying profiles and a continuous decrease in the decay length with increasing frequency. At sufficiently high frequencies, we also observe a regime in which the velocity becomes negative. For viscoelastic materials, we define $\omega_d > \omega_{nl}$ as the frequency above which the system begins to
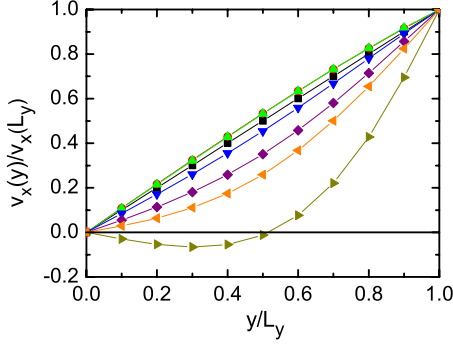
FIG. 3. (Color online) Normalized horizontal velocity profiles $v_x(y)/v_x(L_y)$ at $t=0$ for a viscoelastic material with $\beta=G\rho L_y^2/\eta^2$ $=1$ obtained from solutions to Eq. (1) as a function of the driving frequency ω. We show $\omega/\omega_{nl}=0.1$ (squares), 1.1 (circles), 2.1 (upward triangles), 4.1 (downward triangles), 6.1 (diamonds), 8 (left triangles), and 20 (right triangles). ω_{nl} corresponds to $\omega_{nl}^l=\omega_{nl}^s$.

display monotonically decaying "liquidlike" velocity profiles.

In Fig. 4, we show the total phase shift Δ for the pure liquid and viscoelastic materials as a function of the driving frequency. (The pure solid is not shown since Δ is identically zero for all frequencies.) As expected, Δ for the pure liquid ($\beta=0$) scales linearly with ω. For viscoelastic materials with $\beta>0$, there is a clear crossover from low-frequency scaling $\Delta\sim\omega^n$ to high-frequency scaling $\Delta\sim\omega^m$ with $m<n$. For the Kelvin-Voigt model, the high-frequency limit is equivalent to $G=0$, and $\Delta=\omega/6\omega_{nl}^l$, corresponding to $m=1$, and the low-frequency limit is $\Delta=\omega^3\omega_{nl}^l/(6\omega_{nl}^{s4})$, corresponding to $n=3$. Using these expressions, one can derive the crossover frequency explicitly, $\omega_p=\omega_{nl}^{s2}/\omega_{nl}^l=\omega_{nl}^l\beta$. For a more general model with a complex shear modulus, where the stress is given by $\Sigma_{xy}=G^*(\omega)\gamma$, $G^*(\omega)=G'(\omega)+iG''(\omega)$, and G' and G'' are the storage and loss moduli; the values of n and m depend on the frequency dependence of G' and G''. How-
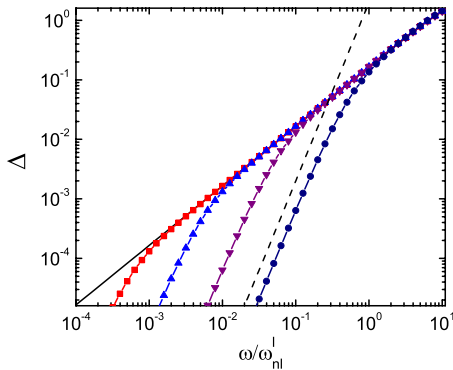

FIG. 4. (Color online) The total phase shift $\Delta=\delta(0)-\delta(L_y)$ for viscoelastic materials with different values of $\beta=G\rho L_y^2/\eta^2$ versus the normalized driving frequency ω/ω_{nl}^l. The curves for all β scale linearly with ω at sufficiently high frequencies. We include $\beta=0$ (solid line), 0.0005 (squares), 0.005 (upward triangles), 0.05 (downward triangles), and 0.5 (filled circles). The crossover frequency ω_p can be obtained by locating the intersection of the low-frequency and high-frequency power-law scaling forms for Δ. The slope of the black solid (dashed) line is 1 (3).
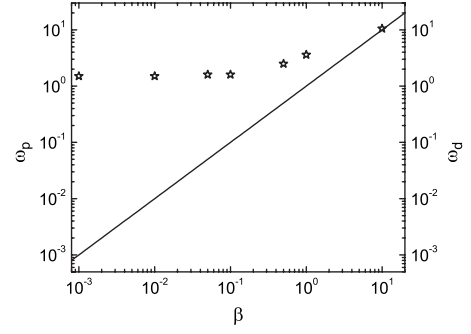

FIG. 5. Plot of ω_p (solid line) and ω_d (stars) versus $\beta=G\rho L_y^2/\eta^2$ for the viscoelastic Kelvin-Voigt model. Note that $\omega_p<\omega_d$ over a wide range of β.

ever, for physically motivated $G^*(\omega)$, the crossover from the low frequency elastically dominated to high-frequency viscously dominated behavior persists. One consequence of the crossover in frequency dependence is that the low-frequency total phase shift tends to zero rapidly at low frequencies, and thus Δ may be difficult to measure at low frequencies in experiments. In our experimental studies, we were able to detect the change in scaling behavior of Δ, but were not able to measure the scaling exponents accurately. Much more sensitive experiments are planned to measure ω_p and the storage and loss moduli at low frequencies.

The dependence of ω_p and ω_d on β for the viscoelastic Kelvin-Voigt model is given in Fig. 5. Here we used the analytical result for ω_p, but ω_d is determined numerically. This figure illustrates an important feature of the model: for $\beta<1$, ω_d is relatively insensitive to β, i.e., whether the system is solid or liquid, while ω_p decreases linearly with β. Thus, as $\beta\to0$, $\omega_p/\omega_d\to0$. This is consistent with the fact that as the system becomes more solidlike, the initial deviations from nonlinearity are positive, so the transition to liquidlike behavior is delayed to higher frequencies. We expect similar behavior for more general models. By measuring these characteristic frequencies, future experimental studies will be able to characterize the material properties of foams and other complex fluids.

It is helpful to summarize the three characteristic frequencies—ω_p, ω_{nl}, and ω_d—that were defined above. ω_p is the crossover frequency that characterizes the change in the scaling behavior of the total phase shift as a function of frequency. For pure solids, ω_p is not defined, for pure liquids, $\omega_p=0$, and for viscoelastic materials $\omega_p>0$. ω_{nl} is the frequency above which we observe deviations from linear behavior in the horizontal velocity profile. For $\omega>\omega_{nl}$, pure liquids display decaying nonlinear velocity profiles with positive curvature and decay more strongly with increasing frequency. In solids and viscoelastic fluids, when $\omega>\omega_{nl}$, the horizontal velocity profile initially possesses negative curvature with deviations "above" the linear velocity profile. Thus, the curvature of the profile at low frequencies near ω_{nl} can be used to differentiate liquidlike from "solidlike" velocity profiles. In the experiments, the solidlike response of the system at low frequencies is weak. Thus, we focus on measuring ω_d, the frequency above which the system begins to display decaying liquidlike velocity profiles (instead of ω_{nl}) and ω_p in the simulations and experiments.

III. SIMULATION METHODS

We performed numerical simulations in 2D of the bubble model, which was generalized to include particles with non-zero mass m, undergoing boundary-driven oscillatory planar shear flow. The systems were composed of a total of $N_t = 1280$ disks with the same mass. Half of the disks were small and the other half were large with diameter ratio $r = 2$ to avoid crystallization under shear and match the bubble distribution used in the bubble raft experiments. The original simulation cell was rectangular with x coordinates in the range $[0, L_x]$ and y coordinates in the range $[-L_y/8, 9L_y/8]$. Bubbles were initialized with random initial positions within this rectangular domain at a given packing fraction ϕ and then the system was relaxed to the nearest local potential-energy minimum using conjugate gradient-energy minimization [31] with periodic boundary conditions in both the x and y directions. All bubbles outside $y = [0, L_y]$ formed two rough rigid boundaries. Bubbles with y coordinates in the range $[L_y, 9L_y/8]$ ($[-L_y/8, 0]$) formed the top (bottom) boundary. $N \approx 1000$ disks filled the interior of the cell between the two rigid boundaries. After the top and bottom boundaries were formed, we used periodic boundary conditions only in the x direction. Packing fractions in the range $\phi = [0.85, 0.9]$ were investigated.

In the bubble model, bubble i experiences two pairwise forces from neighboring bubbles j that overlap i: (1) repulsive linear spring forces that arise from bubble deformation

$$\vec{F}_{ij}^r = \frac{\epsilon}{\sigma_{ij}} \left(1 - \frac{r_{ij}}{\sigma_{ij}} \right) \hat{r}_{ij} \tag{9}$$

and (2) viscous damping forces proportional to the relative velocity between bubbles that arise from dissipation between the fluid walls

$$\vec{F}_{ij}^v = -b(\vec{v}_i - \vec{v}_j), \tag{10}$$

where ϵ sets the energy scale for elastic deformation, $\sigma_{ij} = (\sigma_i + \sigma_j)/2$ is the average diameter, r_{ij} is the center-to-center separation between bubbles i and j, $\hat{r}_{ij} = \vec{r}_{ij}/r_{ij}$ is the unit vector that points from the center of bubble j to the center of bubble i, and b is the damping coefficient. Note that when bubbles i and j do not overlap, the pairwise forces $\vec{F}_{ij}^r = \vec{F}_{ij}^v = 0$.

The ratio of the damping to inertial forces can be expressed via a dimensionless damping coefficient $b^* = b\sigma/\sqrt{\epsilon m}$, where σ is the small bubble diameter. Under-damped (overdamped) systems are characterized by $b^* < b_c^*$ ($b^* > b_c^*$), where $b_c^* = \sqrt{2}$ for linear spring interactions. We studied both under- and overdamped systems in the range $b^* = [0.1, 3]$. The units of energy, length, and time in the simulations are ϵ, σ, and $\sigma/\sqrt{\epsilon/m}$, respectively.

The time evolution of the position $\vec{r}_i$ and velocity $\vec{v}_i$ of an interior bubble i can be obtained by integrating the equation of motion

$$m\frac{d^2\vec{r}_i}{dt^2} = \sum_j (\vec{F}_{ij}^r + \vec{F}_{ij}^v). \tag{11}$$

We employed standard Gear predictor-corrector algorithms to numerically integrate Eq. (11) for the positions and velocities of the interior bubbles [32]. This simple "discrete element" short-range model for 2D foams allows us to quickly and efficiently generate an ensemble of configurations with a given set of external boundary conditions.

Oscillatory planar shear was imposed by rigidly moving all of the bubbles that comprise the top boundary in the x direction as a function of time according to

$$x_b(t) = A \sin(\omega t), \tag{12}$$

while bubbles that comprise the bottom boundary remain stationary. $A = 0.8\sigma$ and ω are the amplitude and angular frequency of the sinusoidal driving. At this amplitude, we did not observe any T1 events [26] over the entire range of driving frequencies studied.

We calculated several important physical quantities in the simulations, including the phase shift of bubble x displacements relative to the motion of the boundary and the horizontal velocity profiles of the bubbles. The x displacements and velocity profiles reached steady state after a few cycles; thus, we began measurements after 5 cycles and continued for an additional 15 cycles to calculate averages. The height dependence of the phase shift and velocity profiles were measured by partitioning the simulation cell into equal-sized rectangular bins centered at y with height $\Delta y \approx 2$ large particle diameters, with y measured from the bottom stationary boundary.

To calculate the local phase shift $\delta(y)$, we averaged the bubble x displacement $u_x(y, t)$ relative to the initial position over all bubbles within the bin located at y. We then fit the average bubble x displacement in each bin to $u_x(y, t) \sim \sin[\omega t - \delta(y)]$ to determine the local phase shift $\delta(y)$. We measured $\delta(y)$ at several times during a given cycle to verify that it was time independent, and the bubble motion was periodic. To measure the average horizontal velocity profile $v_x(y, t)$ of the interior bubbles, we used a binning procedure identical to that employed to measure $\delta(y)$.

An important characteristic time (or frequency) scale in the bubble model is the shear rate $\dot{\gamma}_c$ at which the system transitions from quasistatic behavior at low shear rate (shear stress $\Sigma_{xy} \propto \dot{\gamma}^0$) to highly fluidized behavior at high shear rate ($\Sigma_{xy} \propto \dot{\gamma}^\alpha$, where $\alpha > 0$) when the system is driven by steady planar shear [15]. This frequency scale has also been measured in the bubble raft experiments, and thus $\omega_c = 2\pi\dot{\gamma}_c$ can be used to normalize the crossover frequencies obtained in experiments and simulations. To simulate systems undergoing steady planar shear, we employed the same boundary-driven method as described above except $x_b(t) = L_y\dot{\gamma}t$ instead of Eq. (12). The flow curve for a system with $\phi = 0.86$ and $b^* = 2$ is shown in Fig. 6, where the virial expression including dissipative forces was used to calculate the shear stress [32]. To determine $\dot{\gamma}_c$, we calculated the median of the data point at which the flow curve first deviates by more than 10% from the power-law behavior and the previous data point at higher shear rate. For the flow curve in Fig. 6, we
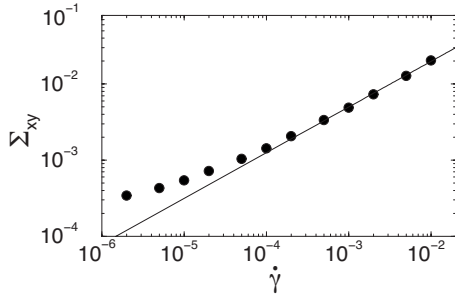
FIG. 6. Average shear stress Σ_{xy} plotted versus the applied shear rate $\dot{\gamma}$ for a system with $\phi=0.86$ and $b^*=2$ undergoing steady planar shear flow in 2D simulations of the bubble model. The crossover shear rate at which the system transitions from quasistatic to power-law behavior is $\dot{\gamma}_c \approx 10^{-4}$.

estimate $\dot{\gamma}_c \approx 2 \times 10^{-4}$. $\dot{\gamma}_c$ was determined for each value of b and ϕ.

IV. EXPERIMENTAL METHODS

The experimental setup to apply oscillatory planar shear to bubble rafts includes three components: a rectangular basin, oscillating paddle, and imaging system. A schematic of the experimental setup is shown in Fig. 7. The basin has dimensions of 37×15 cm^2 and was filled to a depth of 5 cm with a surfactant solution. A paddle was located in the middle of the basin, leaving a span of 9 cm between it and the opposite wall. As illustrated in the schematic in Fig. 7, the ends of the system are "open" in the following sense. The entire basin is filled with bubbles, and the paddle only spans the central portion of the system. Furthermore, only the central third of the bubbles in the region covered by the paddle are used in the data analysis, and thus edge effects are minimized. The paddle was driven by an M-drive 23 stepper motor located outside the basin. A rotor and universal (U-) joint were used to convert the axial drive of the motor into linear sinusoidal motion. The amplitude of oscillation was varied by changing the contact point between the rotor and U joint.

The bubbles were confined between a movable paddle and a fixed wall. The bubbles were constrained to move with the paddle using metal tabs that extended one bubble diameter into the system. The tabs were spaced approximately every five bubbles. The fixed wall consisted of a series of square
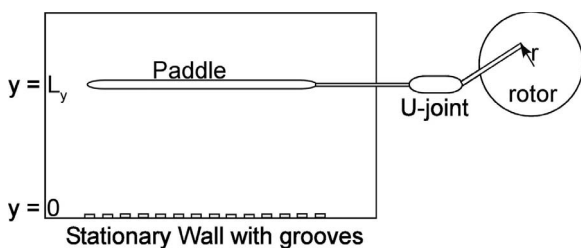

FIG. 7. A schematic of the experimental setup that applied oscillatory planar shear to the bubble rafts. The U joint highlighted in the figure is used to convert the rotary motion of the driving motor into oscillatory planar shear.

indentations approximately the size of a bubble. This fixed the bubble velocities at the stationary wall to zero. Because the first row of bubbles at each wall is interspersed with elements to hold it in place, slight distortions of the bubbles prevented accurate measurement of their positions. Therefore, in the experiments we defined the location of $y=0$ and $y=L_y$ to be the boundary between the first and second rows of bubbles at the stationary wall and paddle, respectively, instead of the location of the physical boundaries. For a sinusoidally oscillating paddle that is initially undisplaced, this gives the boundary condition at $y=L_y$: $x_b(t)=A \sin(\omega t)$, where $A=0.8\sigma$ and ω are the amplitude and frequency of the driving. At this amplitude, no T1 events were recorded over the entire range of ω.

The bubble raft consisted of a bidisperse distribution of bubble sizes: a 4 to 1 ratio of 2.5 ± 0.3-mm- to 5.3 ± 0.5-mm-diameter bubbles, which corresponds to a diameter ratio $r \approx 2.1$. The solution composition was 80% deionized water, 15% glycerol, and 5% miracle bubble (Imperial Toy Corp.), which is a commercially available surfactant. The bubbles were produced by passing compressed nitrogen through the solution via a needle. The diameter of the needle and nitrogen pressure determine the final size of the bubbles. To create bidisperse bubble mixtures, we used two needles with different sizes at constant pressure. After the bubbles were produced, we stirred the solution with a glass rod to break up large-scale crystalline domains, so that only short-range order persisted. We tuned the pressure to prevent multiple layers of bubbles from building up in the z direction.

The definition of the gas (or liquid) area fraction for a bubble raft is somewhat imprecise because the bubbles form three-dimensional (3D) structures on the water surface, which makes it difficult to define the amount of fluid in the walls. Also, using definitions based on T1 events present challenges because true vertices do not exist in bubble rafts, and therefore minimum edge lengths are not well defined. This is in contrast to fully confined two-dimensional systems, such as soap films, for which more precise definitions of liquid area fraction exist [33]. Therefore, for bubble rafts, one typically reports an operational definition of the gas area fraction ϕ as the average cross-sectional area of bubbles that is visible in the images. This is typically done by applying a fixed cutoff to the images to separate pixels inside and outside the bubbles. One expects that this method will provide values for ϕ that approximate the definition of the packing fraction used in the bubble model. Using this operational definition, we find $\phi=0.86 \pm 0.04$ for the bubble raft experiments. The error is estimated based on a range of choices for reasonable cutoff values. As we will show, one advantage of our studies is that they can provide a method for calibrating our definition of the gas area fraction for bubble rafts with the packing fraction for the bubble model.

To visualize the bubble motions, a 210×240 pixel charge-coupled device (CCD) camera was held above the basin. The floor of the basin was constructed from glass, which allowed the entire bubble raft to be illuminated from below by an electroluminescent film (manufactured by Luminous Film Inc.). A frame rate of 60 frames per second was sufficient to capture the bubble motion. The raw experimen-
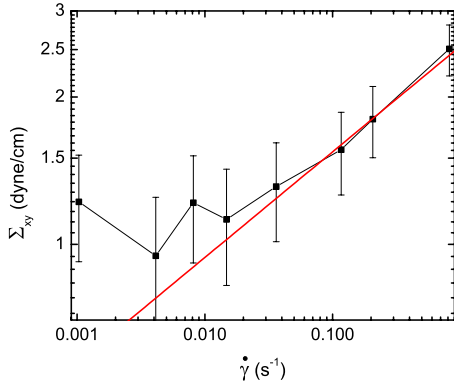
FIG. 8. (Color online) Shear stress Σ_{xy} versus the applied shear rate $\dot{\gamma}$ for the same bubble raft system described in Fig. 1 undergoing steady planar shear. We estimate the crossover frequency $\dot{\gamma}_c \approx 0.065$ s^{-1} above which the system transitions from the quasistatic to the power-law flow regime.

tal images were filtered and thresholded to demarcate the spatial location of each bubble. Further details of the image processing are provided in Refs. [28,29,34].

To measure the velocity profiles, we divided the system in the y direction into ~ 20 equal-sized rectangular bins between $y=0$ and $y=L_y$. The instantaneous velocities of bubbles were then calculated by subtracting the center of mass positions of the bubbles in consecutive image frames for each bin. We employed a particle image velocimetry (PIV) procedure to measure the time evolution of the bubble velocities and thus calculate the phase shift relative to the driving. The horizontal component of the velocity of the interior bubbles can be parametrized by the *rms* velocity $v_{rms} \equiv \sqrt{\langle v_x^2(y) \rangle}$, frequency of oscillation ω, and local phase shift $\delta(y)$ with respect to the moving top boundary. The horizontal
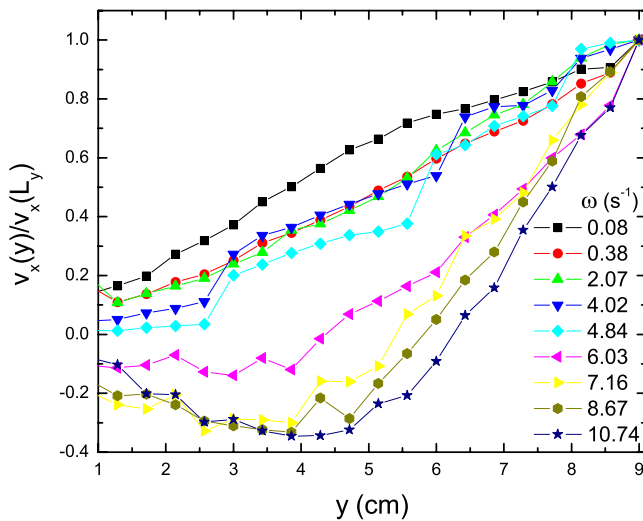

FIG. 9. (Color online) The normalized average horizontal velocity $v_x(y)/v_x(L_y)$ (averaged over times when the boundary velocity is maximum) as a function of distance y from the stationary bottom wall for several driving frequencies ω in the bubble raft experiments. At frequencies $\omega < \omega_d \approx 4.0$ s^{-1}, the profiles are roughly linear, while above this characteristic frequency, liquidlike nonlinear profiles are observed.
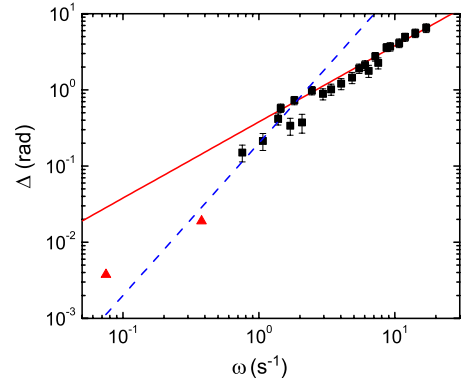

FIG. 10. (Color online) Total phase difference Δ plotted as a function of the driving frequency ω for the bubble raft experiments (black squares). The two triangles represent an upper limit for the measured phase-shift given the resolution of our experiment at the corresponding frequencies. The solid and dashed lines have slopes 1 and 2, respectively. The intersection of these two lines provides a rough estimate for the crossover frequency, $\omega_p \approx 1.9 \pm 0.9$ s^{-1}.

component of the velocity of the interior bubbles is therefore given by

$$v_x(y,t) = v_{mag}(y) \cos[\omega t - \delta(y)], \qquad (13)$$

where $v_{mag} = \sqrt{2} v_{rms}$, which allows us to calculate the local phase shift $\delta(y)$ relative to the moving boundary. In Sec. V below, we will show results for the total phase shift $\Delta \equiv \delta(0) - \delta(L_y)$.

In the oscillatory planar shear experimental setup, we are not able to directly measure the shear stress and thus the flow curve. However, the flow curve has been measured previously for a bubble raft with similar parameters (shown in Fig. 8) [27]. We employed the same method as in the simulations to determine the crossover shear rate $\dot{\gamma}_c \approx 0.065$ s^{-1} at which the system transitions from the quasistatic to the power-law flow regime.

V. EXPERIMENTAL AND SIMULATION RESULTS

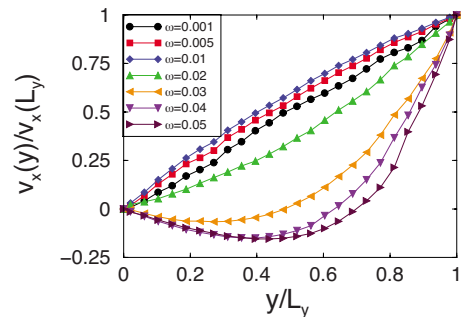In Figs. 9 and 10, we show the results from the experi-

FIG. 11. (Color online) The normalized average velocity $v_x(y)/v_x(L_y)$ (averaged over times when the boundary velocity is maximum) as a function of distance y from the stationary wall plotted for several driving frequencies ω in the bubble model simulations. For $\omega \gtrsim \omega_d \approx 0.02$, the velocity profiles display liquidlike nonlinear decay.
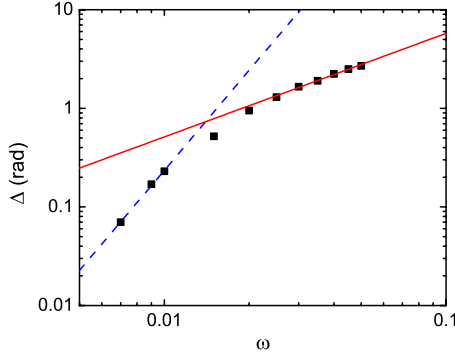
FIG. 12. (Color online) Total phase difference Δ plotted as a function of the driving frequency ω for the bubble model simulations at $\phi=0.86$ and $b^*=2$. From the intersection of the solid red and dashed blue lines with slopes 1 and 3, respectively, we estimate $\omega_p \approx 0.015$.

ments in which bubble rafts were subjected to low-amplitude oscillatory planar shear. Figure 9 displays the horizontal velocity profiles $v_x(y)$ (measured at times when the boundary velocity is maximum as defined in Sec. IV) over a range of driving frequencies. For this system, we find that the velocity profiles transition from nearly linear to liquidlike nonlinear near $\omega_d \approx 4.0 \pm 0.5$ s^{-1}. Note that at the lowest driving frequency, it appears that the velocity profile displays solidlike behavior with slight negative curvature above a linear profile, but this feature is comparable to the size of the fluctuations. Since this feature is difficult to detect and the nonlinear liquidlike profiles are more robust in the experiments, we will focus on measurements of ω_d instead of ω_{nl}.

In Fig. 10, we show measurements of the total phase difference Δ between bubbles near the top and bottom boundaries as a function of the driving frequency. As discussed in Sec. II, for a viscoelastic material we expect a crossover in the scaling of the total phase difference as the driving frequency is increased. For the experiments, we were unable to

fully characterize the crossover behavior due to limits in our ability to measure the phase shift at low frequencies. However, using the maximum possible values of the total phase shift at the lowest frequencies (triangles in Fig. 10), we can set a lower limit on the exponent for the low-frequency scaling regime. This gives us a transition from $\Delta(\omega) \sim \omega^n$ with $n \gtrsim 2$ at low frequencies to linear scaling at high frequencies. Thus, for the bubble raft system, we estimate $\omega_p \approx 1.9 \pm 0.9$ s^{-1}, and thus $\omega_p < \omega_d$.

We also performed simulations of the bubble model undergoing small amplitude oscillatory planar shear over a range of packing fractions ϕ and damping coefficients b^* to compare to the bubble raft experiments. The trend for each set of ϕ and b^* was similar: low-frequency profiles are linear with a nonzero total phase shift followed by a transition to nonlinear liquidlike profiles when $\omega > \omega_d$. In addition, the crossover in the scaling behavior of Δ versus ω was observed. This characteristic behavior is highlighted in Figs. 11 and 12, which show the velocity profiles and total phase shift for the bubble model with $\phi=0.86$ and $b^*=2$. We find $\omega_d \approx 0.02$ and $\omega_p \approx 0.015$ for this set of parameters. In the low-frequency limit, we find $\Delta(\omega) \sim \omega^n$ with $n \approx 2.8 \pm 0.3$ (blue dashed line in Fig. 12), which is similar to the scaling predicted for the Kelvin-Voigt model [35].

Figure 13 summarizes the simulation data (black squares) for the transition to liquidlike nonlinear profiles (ω_d) and the crossover frequency (ω_p). We show both characteristic frequencies ω_d and ω_p at fixed $\phi=0.86$ as a function of b^* including the under- and overdamped regimes and at fixed $b^*=2$ as a function of ϕ. To directly compare the results in experiments and simulations, we normalize ω_d and ω_p by $\omega_c=2\pi\dot\gamma_c$ obtained from the steady planar shear flow curves at each b and ϕ. The experimental results are also displayed in Fig. 13; they are represented as solid lines since ϕ and b^* are not known precisely for the bubble raft experiments. The simulations indicate that at fixed ϕ, the b^* dependence of ω_d/ω_c and ω_p/ω_c is fairly weak as the dissipation switches from underdamped to overdamped. At fixed b^*, both ω_d/ω_c
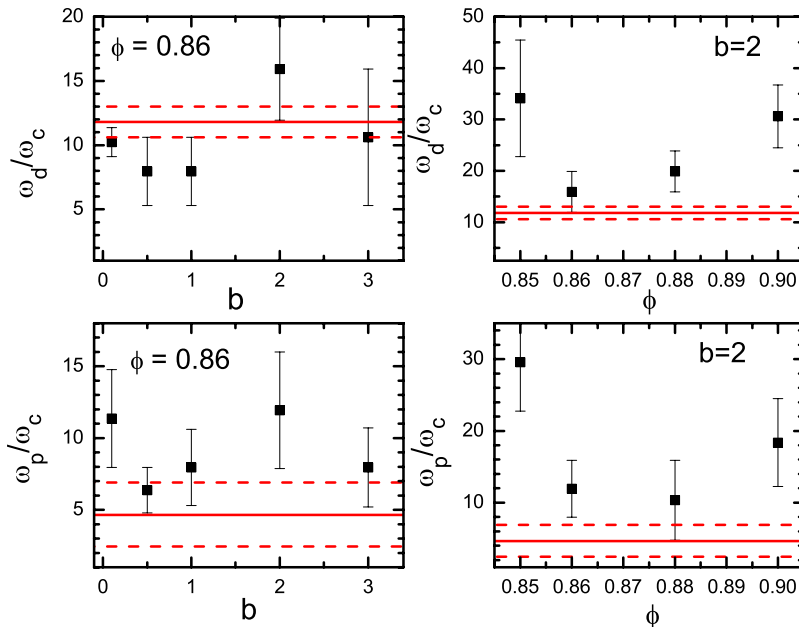
FIG. 13. (Color online) Summary of the measurements of the normalized frequencies ω_d/ω_c (top panels) and ω_p/ω_c (bottom panels) for the bubble model simulations (solid squares) and bubble raft experiments (solid lines). ω_d and ω_p are normalized by ω_c, which is the frequency at which steady planar shear flows crossover from highly fluidized to quasistatic behavior. For the simulations, we show ω_d/ω_c and ω_p/ω_c as functions of b^* at fixed $\phi=0.86$ (left panels) and ϕ at fixed $b^*=2$ (right panels). Because it is difficult to define ϕ and b^* precisely in experiments, the results for the bubble rafts are presented as solid lines (in between dashed lines, which give error bars for the experimental measurements) to identify the range of ϕ and b^* that best fit the experiments.

and ω_p/ω_c increase with packing fraction, if we exclude the first point at $\phi=0.85$.

VI. CONCLUSION

We find that the bubble model captures all of the qualitative features of the response of the bubble rafts to low-amplitude oscillatory planar shear flow. The key elements of the response include: (1) a regime with *linear* velocity profiles, but a nonzero total phase shift at low frequencies, and (2) at the highest frequencies, a regime with liquidlike *nonlinear* profiles and nonzero total phase shift. In addition, in the low-frequency regime, there is a crossover in the scaling of the total phase shift as a function of the driving frequency. The bubble model reproduces each of these distinctive features found in the bubble rafts.

The quantitative agreement shown in Fig. 13 between the simulations and the experiments is also encouraging. In the range of parameters that we expect to correspond most closely to the experiments ($\phi\approx0.86$ and $b^*>\sqrt{2}$), we find agreement to within error bars between the experiment and simulations for the characteristic frequency ω_d at which the system transitions from linear to liquidlike nonlinear velocity profiles, and ω_p, which characterizes the change in scaling of the total phase shift.

The bubble model is often used to characterize highly fluidized flows where T1 bubble rearrangement events occur since it can quantify the statistics of these rearrangement events. It has not been employed as often to quantitatively study slow dense flows where bubble rearrangements are rare since the results can depend on the dissipation model. One of the unique aspects of this study is that it allows a direct comparison between the bubble model and bubble raft experiments in the regime where T1 events and other large-scale bubble rearrangements *do not occur*, which enables stringent tests of the dissipation mechanism in the bubble model. The observed qualitative and quantitative agreements between simulation and experiment provide evidence that the bubble model provides a faithful, yet simple description of dissipation between liquid walls in bubble rafts.

Our focus on the low-amplitude oscillatory shear regime, in the absence of T1 events, provides important insights into the response of foams to applied stress. First, we find that the bubble rafts clearly exhibit dissipative behavior despite the absence of T1 events. This can only be due to motion in the fluid films and emphasizes that further quantitative studies of film-level dissipation mechanisms are crucial to understanding foam rheology [22]. Second, studies of the response of 3D foams and emulsions to oscillatory shear suggest that there are important differences between the two systems in the low-amplitude regime [36–38]. Thus, studying the low-amplitude regime will highlight key differences in the mechanical response of a variety of soft glassy materials. Finally, in this paper we presented results that demonstrate the existence of two additional time (or frequency) scales associated with the response of foam to applied shear: ω_p and ω_d (or ω_{nl}). Thus, we expect that these characteristic time scales will also play a key role in determining the flow curve and velocity profiles for foams undergoing steady planar shear flow.

A quantitative comparison between the bubble raft experiments and bubble model simulations also provides a method to calibrate the gas area fraction of the bubble rafts, which is notoriously difficult to measure in foam experiments. Of the three frequently used quasi-two-dimensional experimental setups (bubble rafts, bubble rafts with a top glass plate, and bubbles confined between two solid surfaces), it is most difficult to define the area fraction in the bubble rafts. By combining the bubble model simulations and surface evolver computations [39,40], it will be possible to define an effective area fraction that will allow direct comparison between bubble raft experiments and other quasi-two-dimensional glassy and jammed systems confined to surfaces and thin films. In the future, we will perform additional experiments over a range of packing fractions, surfactants that yield bubbles with varied elastic properties, and liquid viscosities to investigate whether the predictions of the simple viscoelastic model in Sec. II for the G and η dependences of ω_{nl} and ω_p are valid for the bubble rafts.

[1] D. Weaire and S. Hutzler, *The Physics of Foams* (Claredon Press, Oxford, 1999).

[2] P. Coussot, J. S. Raynaud, F. Bertrand, P. Moucheront, J. P. Guilbaud, H. T. Huynh, S. Jarny, and D. Lesueur, Phys. Rev. Lett. **88**, 218301 (2002).

[3] F. Varnik, L. Bocquet, J.-L. Barrat, and L. Berthier, Phys. Rev. Lett. **90**, 095702 (2003).

[4] A. Kabla and G. Debrégeas, Phys. Rev. Lett. **90**, 258303 (2003).

[5] J. Lauridsen, G. Chanan, and M. Dennin, Phys. Rev. Lett. **93**, 018303 (2004).

[6] N. Xu, C. S. O'Hern, and L. Kondic, Phys. Rev. Lett. **94**, 016001 (2005).

[7] N. Xu, C. S. O'Hern, and L. Kondic, Phys. Rev. E **72**, 041504 (2005).

[8] C. Gilbreth, S. Sullivan, and M. Dennin, Phys. Rev. E **74**, 051406 (2006).

[9] E. Janiaud, D. Weaire, and S. Hutzler, Phys. Rev. Lett. **97**, 038302 (2006).

[10] R. J. Clancy, E. Janiaud, D. Weaire, and S. Hutzler, Eur. Phys. J. E **21**, 123 (2006).

[11] G. Katgert, M. E. Möbius, and M. van Hecke, Phys. Rev. Lett.

101, 058301 (2008).

[12] A. Wyn, I. T. Davies, and S. J. Cox, Eur. Phys. J. E **26**, 81 (2008).

[13] L. D. Landau and E. M. Lifshitz, *Fluid Mechanics*, Course of Theoretical Physics Vol. 6, 2nd ed. (Butterworth-Heinemann, Washington, DC, 1987).

[14] S. Hutzler, D. Weaire, and F. Bolton, Philos. Mag. B **71**, 277 (1995).

[15] D. J. Durian, Phys. Rev. E **55**, 1739 (1997).

[16] Y. Jiang, P. J. Swart, A. Saxena, M. Asipauskas, and J. A. Glazier, Phys. Rev. E **59**, 5819 (1999).

[17] S. Tewari, D. Schiemann, D. J. Durian, C. M. Knobler, S. A. Langer, and A. J. Liu, Phys. Rev. E **60**, 4385 (1999).

[18] M. Dennin and C. M. Knobler, Phys. Rev. Lett. **78**, 2485 (1997).

[19] A. D. Gopal and D. J. Durian, Phys. Rev. Lett. **75**, 2610 (1995).

[20] M. Dennin, Phys. Rev. E **70**, 041406 (2004).

[21] T. Okuzono and K. Kawasaki, Phys. Rev. E **51**, 1246 (1995).

[22] N. D. Denkov, S. Tcholakova, K. Golemanov, K. P. Ananthapadmanabhan, and A. Lips, Phys. Rev. Lett. **100**, 138301 (2008).

[23] L. Bragg and W. M. Lomer, Proc. R. Soc. London, Ser. A **196**, 171 (1949).

[24] D. J. Durian, Phys. Rev. Lett. **75**, 4780 (1995).

[25] A. S. Argon and H. Y. Kuo, Mater. Sci. Eng. **39**, 101 (1979).

[26] M. Lundberg, K. Krishan, N. Xu, C. S. O'Hern, and M. Dennin, Phys. Rev. E **77**, 041505 (2008).

[27] E. Pratt and M. Dennin, Phys. Rev. E **67**, 051402 (2003).

[28] Y. Wang, K. Krishan, and M. Dennin, Phys. Rev. E **73**, 031401 (2006).

[29] Y. Wang, K. Krishan, and M. Dennin, Phys. Rev. Lett. **98**, 220602 (2007).

[30] A. M. Kosevich, E. M. Lifshitz, L. D. Landau, and L. P. Pitaevskii, *Theory of Elasticity*, Course on Theoretical Physics Vol. 7, 3rd ed. (Butterworth-Heinemann, Washington, DC, 1986).

[31] W. H. Press, B. P. Flannery, S. A. Teukolsky, and W. T. Vetterling, *Numerical Recipes in FORTRAN 77* (Cambridge University Press, New York, 1986).

[32] M. P. Allen and D. J. Tildesley, *Computer Simulation of Liquids* (Oxford University Press, New York, 1987).

[33] C. Raufaste, B. Dollet, S. Cox, Y. Jiang, and F. Graner, Eur. Phys. J. E **23**, 217 (2007).

[34] F. Krishan, http://www.physics.uci.edu/~foams/

[35] In the bubble model simulations, we have performed preliminary measurements of the frequency-dependent storage and loss moduli, $G'(\omega)$ and $G''(\omega)$. We find that the linear-response regime occurs for $A < 0.5\sigma$. Despite this, we find that the scaling behavior of ω_p with frequency is consistent with the Kelvin-Voigt model.

[36] A. Saint-Jalmes and D. J. Durian, J. Rheol. **43**, 1411 (1999).

[37] S. Cohen-Addad, H. Hoballah, and R. Höhler, Phys. Rev. E **57**, 6897 (1998).

[38] S. A. Khan, C. A. Schnepper, and R. C. Armstrong, J. Rheol. **32**, 69 (1988).

[39] K. A. Brakke, Philos. Trans. R. Soc. London, Ser. A **354**, 2143 (1996).

[40] S. J. Cox and E. Janiaud, Philos. Mag. Lett. **88**, 693 (2008).